Astronomy & Astrophysics manuscript no. ms
August 23, 2016
© ESO 2016

arXiv:1608.06118v1 [astro-ph.HE] 22 Aug 2016

Accretion regimes in the X-ray pulsar 4U 1901+03

P. Reig[1,2] and F. Milonaki[2]

[1] IESL, Foundation for Reseach and Technology-Hellas, 71110, Heraklion, Greece
[2] Physics Department, University of Crete, 71003, Heraklion, Greece e-mail: pau@physics.uoc.gr

Received ; accepted

ABSTRACT

Context. The source 4U 1901+03 is a high-mass X-ray pulsar than went into outburst in 2003. Observation performed with the Rossi X-ray Timing Explorer showed spectral and timing variability, including the detection of flares, quasi-periodic oscillations, complex changes in the pulse profiles, and pulse phase dependent spectral variability.
Aims. We re-analysed the data covering the 2003 X-ray outburst and focused on several aspects of the variability that have not been discussed so far. These are the 10 keV feature and the X-ray spectral states and their association with accretion regimes, including the transit to the propeller state at the end of the outburst.
Methods. We extracted light curves and spectra using data from the Rossi X-ray Timing Explorer. Low time resolution light curves were used to create hardness-intensity diagrams and study daily changes in flux. High time resolution light curves were used to create pulse profiles. An average spectrum per observation allowed us to investigate the evolution of the spectral parameters with time.
Results. We find that 4U 1901+03 went through three accretion regimes over the course of the X-ray outburst. At the peak of the outburst and for a very short time, the X-ray flux may have overcome the critical limit that marks the formation of a radiative shock at a certain distance above the neutron star surface. Most of the time, however, the source is in the subcritical regime. Only at the end of the outburst, when the luminosity decreased below $\sim 10^{36}$ $(d/10\,\mathrm{kpc})^2$ erg s^{-1}, did the source enter the propeller regime. Evidence for the existence of these regimes comes from the pulse profiles, the shape of the hardness-intensity diagram, and the correlation of various spectral parameters with the flux. The 10 keV feature appears to strongly depend on the X-ray flux and on the pulse phase, which opens the possibility to interpret this feature as a cyclotron line.

Key words. stars: individual: 4U 1901+03, – X-rays: binaries – stars: neutron – stars: binaries close –stars: emission line, Be

1. Introduction

The source 4U 1901+03 was first detected in X-rays by the *Uhuru* mission in 1970-1971. New *Uhuru* observations failed to detect the source a year later (Forman et al. 1976). 4U 1901+03 was not detected again until February 2003, when the source underwent a giant X-ray outburst that lasted for about five months and in which the X-ray luminosity changed by almost three orders of magnitude from $\sim 10^{38}$ erg s^{-1} to $\sim 10^{35}$ erg s^{-1}, assuming a distance of 10 kpc (Galloway et al. 2005). Renewed X-ray activity was detected by *MAXI*/GSC (Sootome et al. 2011) and *Fermi*/GBM (Jenke & Finger 2011) in 2011. However, the 2011 event was a short ($\sim$ 1 month) and weak event with a maximum intensity of $\sim$23 mCrab in the energy range 4–10 keV on MJD 55920 (Sootome et al. 2011), more than two orders of magnitude lower than the peak of the 2003 event.

The source 4U 1901+03 is believed to be a Be/X-ray binary (BeXB), although no optical counterpart has been detected so far. Evidence for this classification comes exclusively from its X-ray timing properties. 4U 1901+03 is a transient X-ray pulsar with a pulse period of 2.76 seconds (Galloway et al. 2005). The orbital period of 22.6 days (Galloway et al. 2005; Jenke & Finger 2011) locates 4U 1901+03 in the region populated by BeXBs of the $P_{\rm orb} - P_{\rm spin}$ diagram (Corbet 1986). A quasi-periodic oscillation (QPO) was detected by James et al. (2011). The frequency of the QPO ($\sim$ 0.135 Hz) lies in the milliHertz range, in agreement with other BeXB pulsars (Paul & Naik 2011, and references therein). The pulse profile is complex and displays variability over the course of the outburst. At high luminosity, it shows a double-peak structure that changes into single peak towards the end of the outburst. These changes were interpreted as a change from an accretion column dominated by radiative shock above the neutron star surface (fan beam) into a configuration where the accreted mass is decelerated on to the surface of the neutron star (pencil beam) (Chen et al. 2008). Pulse-phase spectroscopy showed that the main pulse peak has the hardest spectrum, which is a common property of accreting pulsars (Lei et al. 2009).

The X-ray spectrum shows significant emission above 10 keV, which would also agree with an accreting pulsar (Molkov et al. 2003; Galloway et al. 2005). However, the flux decreases quickly with energy; there is little emission above 80 keV, in contrast to many high-mass X-ray pulsars. Attempts to fit the X-ray spectrum over the entire outburst with a consistent model at high as well as low luminosity have proved to be difficult. An absorbed power-law and exponential cutoff (Molkov et al. 2003; James et al. 2011) or a model consistent with thermal Compotonization (Galloway et al. 2005) leave residuals, especially at around 10 keV, indicating that these models do not completely describe the source spectrum.

Accreting X-ray pulsars go through different accretion regimes associated with the X-ray luminosity. Observational evidence for the existence of these accretion regimes comes from the shape of the pulse profiles (Basko & Sunyaev 1976; Parmar et al. 1989), the correlation between the energy of cyclotron lines and flux (Becker et al. 2012; Poutanen et al. 2013; Nishimura 2014; Mushtukov et al. 2015b), and the dependence

Send offprint requests to: pau@physics.uoc.gr

of the X-ray continuum with luminosity (Reig & Nespoli 2013; Postnov et al. 2015).

In this work, we revisit the Rossi X-ray Timing Explorer (*RXTE*) observations and perform a new timing and spectral analysis with emphasis on the residuals at ∼ 10 keV. We study the X-ray variability of 4U 1901+03 in the context of accretion regimes. Finally, we investigate the X-ray spectrum at very low accretion rates, where an abrupt decrease in flux is observed, which might be associated with a transition to the propeller state. We also perform an optical and infrared photometric analysis in an attempt to determine its optical counterpart.

2. Observations

2.1. X-ray observations

The *RXTE* data consist of 64 observation intervals covering the period JD 2452680.3 (10 February 2003) to JD 2452836.9 (16 July 2003). *RXTE* carried three instruments: the All Sky Monitor (ASM) (Levine et al. 1996), the Proportional Counter Array (PCA Jahoda et al. 2006), and the High Energy X-ray Timing Experiment (HEXTE Rothschild et al. 1998). In this work, the timing analysis was performed using data from the PCA, while for the spectral analysis we used both the PCA and HEXTE data.

The PCA covered the energy range 2–60 keV and consisted of five identical coaligned gas-filled proportional units giving a total collecting area of 6500 cm2 and providing an energy resolution of 18% at 6 keV. The HEXTE was constituted by two clusters of four NaI/CsI scintillation counters, with a total collecting area of 2 × 800 cm2, which are sensitive in the 15–250 keV band with a nominal energy resolution of 15% at 60 keV.

Owing to the low Earth orbit of *RXTE*, the observations consisted of a number of contiguous data intervals or pointings interspersed with observational gaps produced by Earth occultations of the source and passages of the satellite through the South Atlantic Anomaly. Data taken during satellite slews, passage through the South Atlantic Anomaly, Earth occultation, and high voltage breakdown were filtered out.

2.2. Optical observations and infrared data

In an attempt to identify the optical counterpart to 4U 1901+03, we obtained optical photometry in three broad bands, *B*, *V*, and *R* (Bessell 1990), and a narrow Hα filter. The observations were made with the 1.3 m telescope of the Skinakas observatory on the night of 22 July 2015 using a 2048×2048 ANDOR CCD with a 13.5 μm pixel size (corresponding to 0.28 arcsec on the sky) and thus providing a field of view of ∼9.5 arcmin squared.

The instrumental magnitudes were used to construct a colour-colour ($R-$Hα vs $B-V$) diagram following the procedure described in Reig et al. (2005). Be stars are expected to occupy the upper (because they are Hα emitters) and left (because they are early-type objects). Additionally, potential candidates should lie inside the X-ray uncertainty region.

We also used the 2MASS catalogue (Skrutskie et al. 2006) to compute the reddening-free quantity $Q = (J-H) - 1.70(H-K_S)$ to create a Q/K_S diagram (Negueruela & Schurch 2007). This diagram is useful to separate early-type from late-type stars. The majority of stars in Galactic fields are concentrated around $Q = 0.4 - 0.5$, corresponding to field K and M stars, while early-type stars typically have $Q \lesssim 0$. We filtered out the infrared data and considered only the best-quality detections, with signal-to noise ratios higher than 7 and uncertainties of less than 0.155 mag (Q-flag equal to A or B) and without contamination or confusion from nearby sources (C-flag equal 0). Typical errors for K_S and Q are 0.05 and 0.1 mag., respectively.

Figure 1 shows the optical colour-colour and the infrared Q/K_S diagrams. The blue and red boxes in the right panel of this figure denote the area where Be and early-type supergiant stars are expected to appear, respectively (Negueruela & Schurch 2007). These candidates are represented in Fig. 2 by red and blue circles, while the candidates from the optical colour-colour diagram are indicated by purple circles. The optical photometry did not provide any strong candidate. All potential candidates are far away from the *RXTE* X-ray error circle. The infrared data mark stars 165 and 417 as possible candidates for a Be star (Fig. 2). However, star 165 (V=15.4 mag) does not stand out in the optical diagram (red empty square). We note that the infrared observations were made many years before the optical observations. Be stars are known to go through active (with a well-developed equatorial disk) and disk-loss phases on timescales of years. Therefore, star 165 might still be the correct counterpart if it were found to be in a low phase (without the disk) during the optical observations. Star 417 was too faint to obtain photometry trough the Hα filter.

We obtained a low-resolution (2 Å/pixel) optical (3500-7300 Å) spectrum of star 165 from the Skinakas observatory on 23 June 2016. Balmer lines in absorption are the most prominent features. The presence of weak HeI lines at 4016 Å, 4713 Å, and 4921 Å cannot be ruled out, although HeI 6678 Å is not seen. Overall, the optical spectrum resembles that of a late B-type star (later than B5) or early A-type star. The equivalent width of the Hα and *H*β lines (12 Å and 15 Å, respectively) would confirm this classification (Jaschek & Jaschek 1987). The lack of strong OII lines precludes a supergiant star, although a slightly evolved star (luminosity class III) cannot be excluded. Although it is unlikely that star 165 is the optical counterpart, a higher resolution spectrum with a higher signal-to-noise ratio, especially in the blue part, is needed to clarify its spectral type.

3. Results

The information on the X-ray pulsar 4U 1901+03 is basically limited to the *RXTE* observations. The analysis of these observations allowed the discovery of pulsations and the determination of the orbital parameters (Galloway et al. 2005), the study of the pulse profile variability, both with time and energy (Chen et al. 2008; Lei et al. 2009), and the detection of a QPO (James et al. 2011). We have preformed a correlated X-ray timing and spectral analysis to study whether this source exhibits spectral states as it evolves through the X-ray outburst. The presence of states has been associated with different accretion regimes (Reig & Nespoli 2013). In addition to the super- and sub-critical regimes, we also examined whether 4U 1901+03 transited to the propeller regime at the end of the outburst.

3.1. Hardness-intensity diagram

For each of the individual X-ray observations, we extracted light curves and spectra. The average intensity of each observation was used to study the evolution over time and to create colour-intensity diagrams (HID). A HID is a plot of the X-ray intensity as a function of hardness. The hardness ratio is the ratio between the photon counts in two broad energy bands. Figure 3 shows the light curve of the outburst and the HID constructed with a hardness ratio defined by the 4–7 keV and 7–10 keV energy bands.

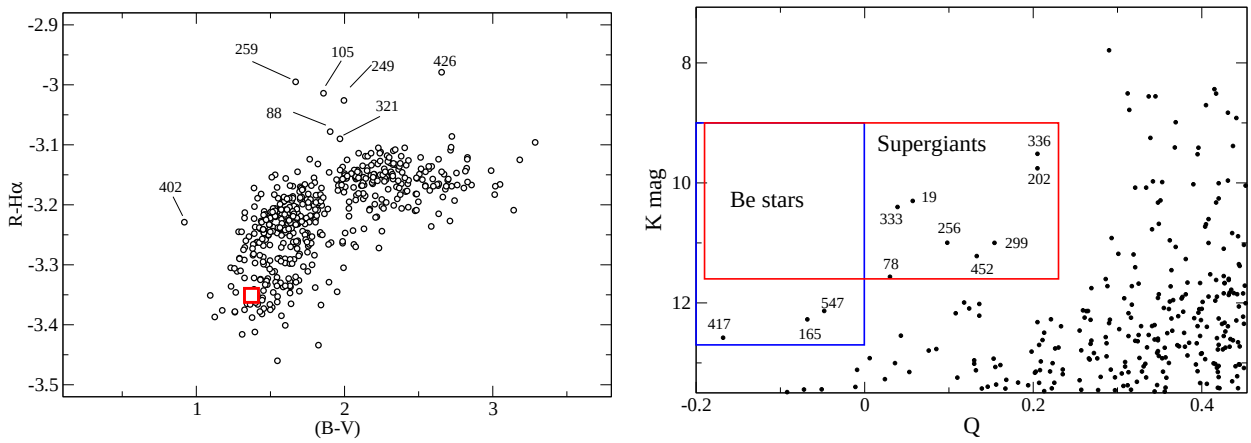

Fig. 1. Optical and infrared diagrams used to search for the optical counterpart. The star represented with a red empty square in the left panel corresponds to star 165 from the infrared data. The blue and red boxes in the right panel denote the area occupied by Be and early-type supergiant stars, respectively.

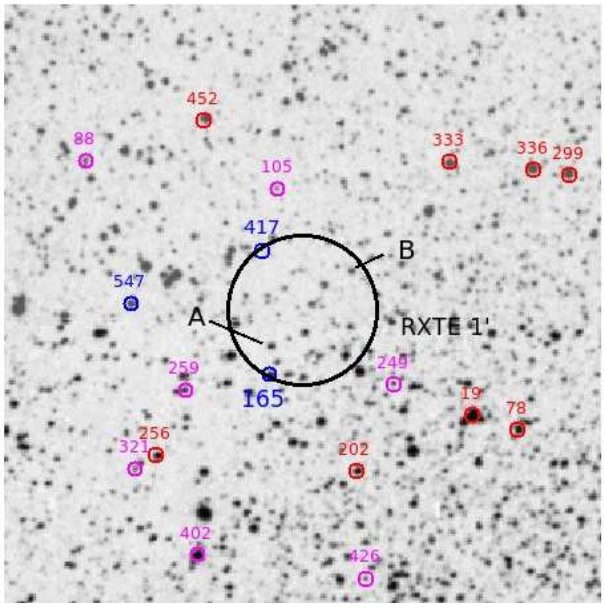

Fig. 2. Identification of candidates. Red and blue circles correspond to possible candidates according to the position in the Q/K_S diagram, while purple circles correspond to candidates from the optical diagram. The image size is $8.5' \times 8.5'$. The X-ray position is R.A. = 19h03m37s.1, Decl. = +3 11'31" (equinox 2000.0; estimated 1' uncertainty at 90% confidence Galloway et al. 2003). Stars A and B are not the optical counterpart because they are late-type stars (Galloway et al. 2005). Image taken from the Digitized Sky Survey (DSS), available through the Skyview Virtual Observatory (http://skyview.gsfc.nasa.gov/current/cgi/titlepage.pl)

The first PCA observation was made ∼10 days before the source reached the peak of the outburst. During this short rise, the source moved toward the right (i.e. hardened) in the HID. As the count rate decreased following the decay of the outburst, the spectrum became softer. A deviation from a smooth decay is recorded at around ∼70 c s^{-1}, in which the source suddenly became harder (Fig. 3). The lowest flux points correspond to the softest spectrum.

3.2. X-ray spectra

An energy spectrum was obtained for each pointing. We used Standard 2 mode data from the PCA (PCU2 only) and Standard (archive) mode from the HEXTE Cluster A, with a time resolution of 16 s. The PCA and HEXTE spectra were extracted, background-subtracted, and dead-time corrected. For the PCA, the 3–30 keV energy range was retained, while the HEXTE provided a partially overlapping extension from 25 to 100 keV. A systematic error of 0.6% was added quadratically to the statistical one. The two resulting spectra were simultaneously fitted with XSPEC v. 12.8.0 (Arnaud 1996).

The X-ray spectra were fitted with a multi-component model consisting of an absorbed (`PHABS` in XSPEC terminology) power law and exponential cutoff (`CUTOFFPL`) plus two discrete components: an emission line at 6.4 keV representing fluorescent iron line emission and a broad absorption component around 10 keV. These two components were modelled with Gaussian profiles (`GAUSS` and `GABS`, respectively). Therefore the model consisted of the following spectral parameters: hydrogen column density, N_H, exponent of the power law or photon index, Γ, cut-off energy, $E_{\rm cut}$, and the line energy and width of the two Gaussians, $E_{\rm Fe}$, $E_{\rm abs}$, $\sigma_{\rm Fe}$, and $\sigma_{\rm abs}$. In addition, each of these components has a normalisation coefficient. For the Gaussian lines, the normalisation (or line depth) is related to the optical depth, which at the line centre is $\tau_{\rm c} = {\rm norm}/(\sqrt{2\pi}\,\sigma_{\rm abs})$. The photon distribution of each model component is given in Table 1. To account for inter-calibration uncertainties between the two instruments, a constant factor was introduced. This factor was fixed to one for the PCA data and allowed to vary freely for the HEXTE data. At low flux ($\sim 5\times10^{-10}$ erg cm^{-2} s^{-1} or $L_X \sim 6\times10^{36}$ erg s^{-1}, assuming a distance of 10 kpc), the signal-to-noise ratio of the continuum deteriorates and the spectrum is consistent with a simple power law, where neither the cut-off nor the broad Gaussian components are required to obtain an acceptable fit.

Soft X-rays are absorbed by the interstellar medium through the photoelectric effect (Morrison & McCammon 1983; Balucinska-Church & McCammon 1992). Because of the steep energy dependence of the cross-section with the abundances assumed for the Galaxy (Anders & Grevesse 1989), photoelectric absorption is significant at energies below ∼ 1 keV. Initially, the hydrogen column density was let free to vary. Its value remained roughly constant at a value of 3.5×10^{22} cm^{-2} during most of the

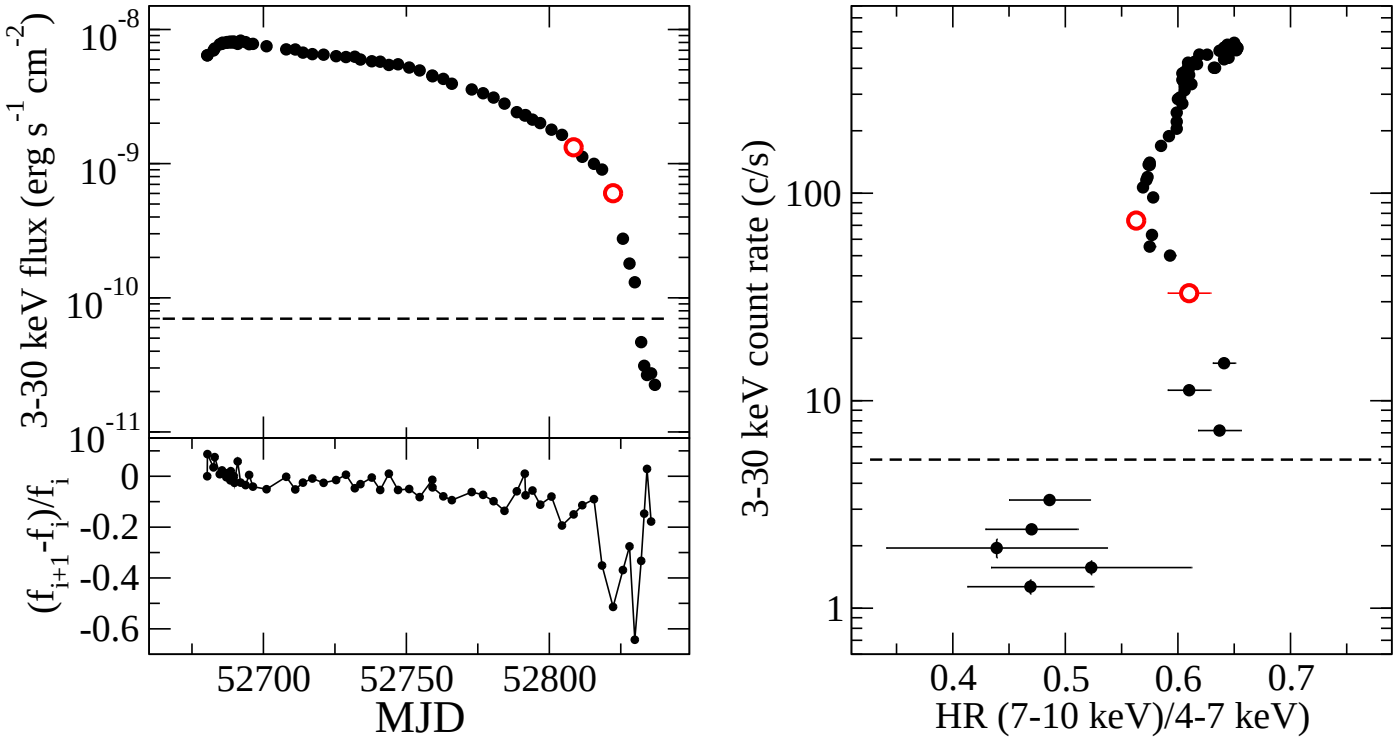

Fig. 3. *Left*: X-ray flux. Each point represents the average of one observation. *Right*: Hardness-intensity diagram. The horizontal dashed line marks the lowest flux below which the source is expected to enter the propeller regime. Open circles indicate the breaks in the light curves and HID.

outburst and displayed a small decrease towards low-flux observations. Because the trend is not statistically significant and the PCA instrument cannot constrain this parameter well (it is sensitive for energies above 3 keV), we set $N_H = 3.3 \times 10^{22}$ cm^{-2} and kept it fixed during the fitting procedure.

The photon index and cut-off energy anti-correlate with the X-ray flux (Fig. 4). The hardest spectrum is seen at the peak of the outburst.

Iron line emission is commonly observed in the X-ray spectra of accreting X-ray pulsars (Torrejón et al. 2010; Giménez-García et al. 2015). The most likely origin is Fe K line fluorescence that is produced as a consequence of the X-ray illumination of matter. The result that we find for 4U 1901+03 agrees with those observed in other BeXBs (Reig & Nespoli 2013): *i)* the energy of the iron line did not change significantly and is consistent with cold non-ionised iron. The average and standard deviation of the line energy is $E_{\rm Fe} = 6.5 \pm 0.1$ keV, *ii)* the flux of the line is well correlated with the flux of the continuum, and *iii)* the equivalent width is insensitive to luminosity changes (Fig. 5). The line width close to the peak of the outburst appears to be somewhat broader $\sigma = 0.8 \pm 0.3$ keV. Below 8×10^{-9} erg cm^{-2} s^{-1} the width is consistent with a narrow line ($\sigma < 0.5$ keV). However, given the modest spectral resolution of the PCA, good fits were obtained by fixing the width at $\sigma_{\rm Fe} = 0.5$ keV in all observations. To better constrain the spectral parameters of the power law, cut-of,f and absorption feature, we fixed the energy of the iron line and width to 6.5 keV and 0.5 keV, respectively, during the extraction of the spectral continuum parameters and the estimation of their errors.

Table 1. Photon distributions of the phenomenological models used in the spectral analysis.

XSPEC model	Photon energy distribution
PHABS	$A(E) = e^{-N_{\rm H}\sigma_{MM}(E)}$
CUTOFFPL	$C(E) = K\,E^{-\Gamma}e^{-E/E_{\rm cut}}$
POWER	$P(E) = K\,E^{-\Gamma}$
HIGHECUT	$H(E) = 1\ E \leqslant E_{\rm cut}$; $H(E) = e^{(E_{\rm cut}-E)/E_{\rm fold}}\ E \geqslant E_{\rm cut}$
GAUSS	$G(E) = K_1 \frac{1}{\sigma\sqrt{2\pi}} e^{-0.5\left(\frac{E-E_l}{\sigma}\right)^2}$
GABS	$G_{\rm abs}(E) = e^{\left(-K_2 \frac{1}{\sigma_0\sqrt{2\pi}} e^{-0.5\left(\frac{E-E_0}{\sigma_0}\right)^2}\right)}$
EDGE	$M(E) = 1\ E \leqslant E_c$; $M(E) = e^{-D(E/E_c)^{-3}}\ E \geqslant E_c$
COMPTT	see Titarchuk (1994); Hua & Titarchuk (1995)
COMPMAG	see Farinelli et al. (2012)

$\sigma_{MM}(E)$: 0.03-10 keV interstellar photoelectric absorption cross-section (Morrison & McCammon 1983).
$N_{\rm H}$: equivalent hydrogen column.
K: normalisation in photons keV^{-1} cm^{-2} s^{-1} at 1 keV.
Γ: power-law photon index.
$E_{\rm cut}$: cut-off energy in keV.
$E_{\rm fold}$: folding energy in keV.
E_l: iron line energy in keV.
σ: iron line width in keV.
K_1: total photons cm^{-2} s^{-1} in the line.
E_0: central energy of the absorption line in keV.
σ_0: width of the absorption line in keV.
$\tau_0 = K_2/(\sqrt{2\pi}\,\sigma_0)$, optical depth of the absorption line.
E_c: threshold energy
D: absorption depth at the threshold

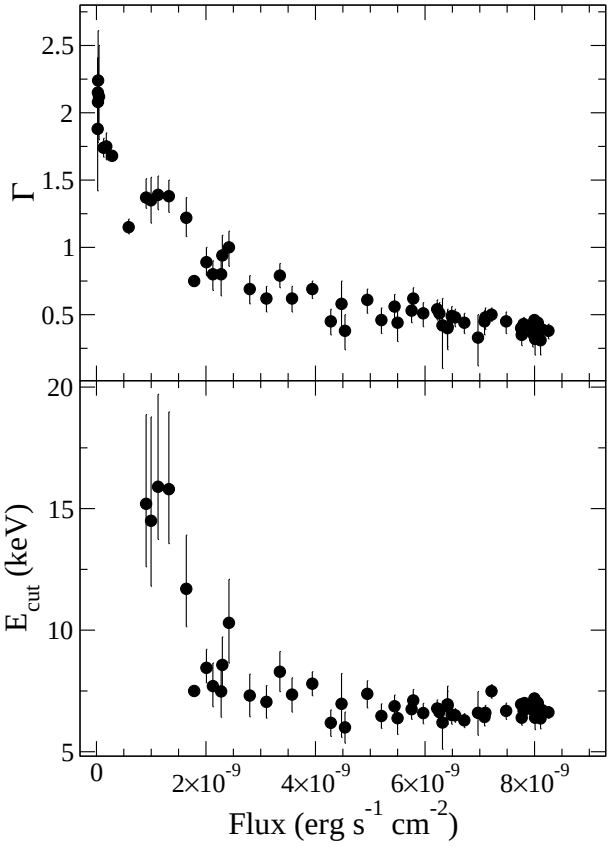

Fig. 4. Evolution of the photon index and cutoff energy as a function of the 3–30 keV flux.

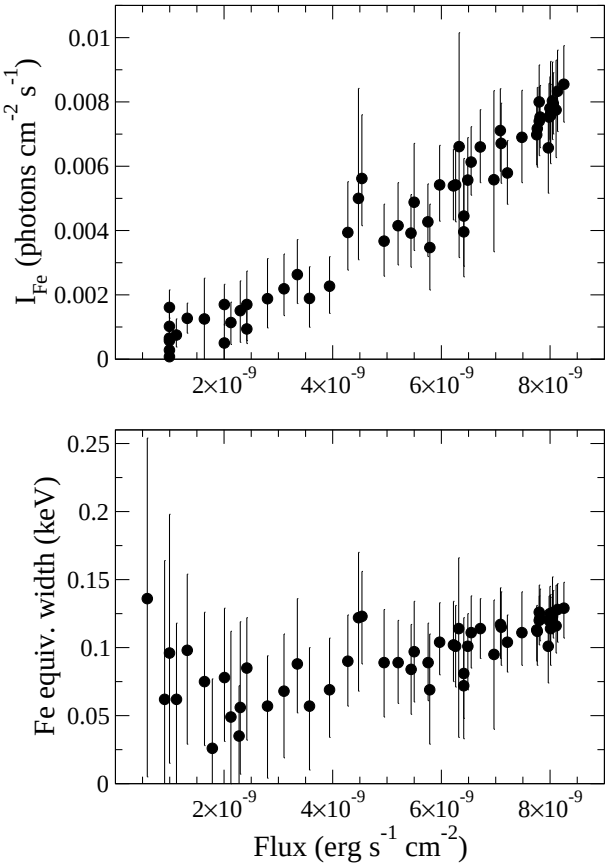

Fig. 5. Iron line flux and equivalent width as a function of continuum the 3–30 keV X-ray flux.

3.3. 10 keV feature

The 10 keV feature is a component that we found in all the spectra of 4U 1901+03 with an X-ray flux above $\sim 5 \times 10^{-10}$ erg cm^{-2} s^{-1} ($L_X \sim 6 \times 10^{36}$ erg s^{-1}, assuming a distance of 10 kpc). Without this component, the fits were unacceptable (see Fig 6). Below this limit the spectra are too noisy and the component is not statistically significant. Its central energy increases as the flux increases (Fig. 7). This clear correlation and the relatively large amplitude change (a factor of two) in $E_{\rm abs}$ motivated us to investigate further whether the absorption feature that we observed in 4U 1901+03 can be attributed to a cyclotron resonant scattering feature (CRSF). We followed three lines of action: *i)* we checked whether the 10 keV feature in 4U 1901+03 is an instrumental effect, *ii)* we investigated whether it might result from improper continuum fitting, and *iii)* we performed pulse-resolved spectroscopy.

One way to discard an instrumental origin for this feature is to compare the spectrum of 4U 1901+03 with that of the Crab nebula. The Crab nebula is a well-known calibration source with a pure power-law spectrum, without any other features (Weisskopf et al. 2010), at least in the PCA energy band. We selected the Crab nebula observation made on 13 February 2003 (OBSID 70802-01-08-00) to be close to the observations of 4U 1901+03. We extracted the X-ray spectrum using the same configuration as the source (see Sect. 3). The best fit (χ^2 = 50.6 for 52 degrees of freedom) was achieved with an absorbed power law with a hydrogen column density $N_H = (0.4 \pm 0.1) \times 10^{22}$ cm^{-2}, photon index $\Gamma = 2.104 \pm 0.007$, and normalisation 10.6 ± 0.2 photons keV^{-1}cm s^{-1} at 1 keV. No residuals are apparent at or around 10 keV. Thus we conclude that the deficit of photons at around 10 keV is not an instrumental effect.

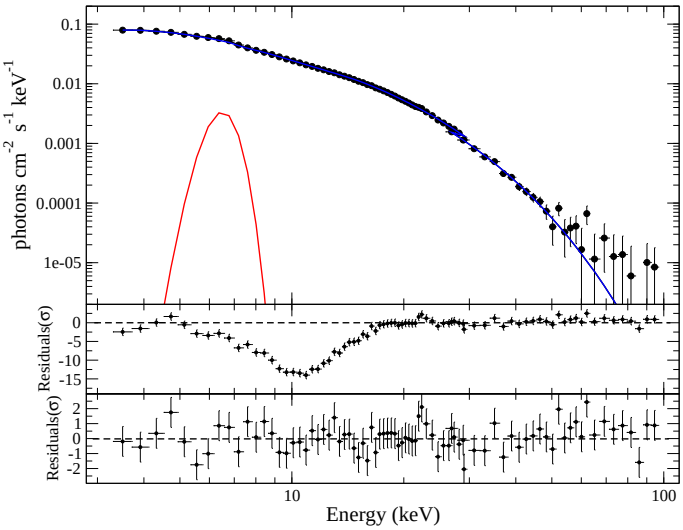

Fig. 6. X-ray spectrum of 4U 1901+03 on 2003-02-12 (OBSID 70096-01-01-03). The middle panel shows the residual when the `GABS` component is not included in the fit. The bottom panel shows the residuals for the best-fit model.

To check whether the residuals around 10 keV could be caused by improper model fitting of the continuum, we tried different combinations of model components. The photon distribution of the various phenomenological models are given in Table 1. We also tried more physical models that explain

the X-ray continuum of pulsars as inverse Comptonization of low-energy photons. Here we used the model developed by Hua & Titarchuk (1995), which describes Comptonization of soft photons in a hot plasma (named COMPTT in XSPEC), and which is the one used by Galloway et al. (2005), and that of Farinelli et al. (2012), which describes the spectral formation in the accretion column onto the polar cap of a magnetized neutron star, with both thermal and bulk Comptonization processes taken into account (COMPMAG in XSPEC). When phenomenological models were used, the spectra were fitted with the function $f(E)$ = PHABS $*$ (COMP1 + GAUSS) $*$ COMP2, where COMP1 is CUTOFFPL or POWER*HIGHECUT and COMP2 GABS or EDGE. When Comptonization models were used, the spectra were fitted with the function $f(E)$ = PHABS $*$ (COMPTOM + GAUSS), where COMPTOM refers to one of the two Comptonization models shown in Table 1. For this analysis, we used the observation made on February 19, 2003 (obsid 70068-22-01-04), but other high or moderate flux observations produced the same result. We found the following results:

- The replacement of CUTOFFPL by POWER*HIGHECUT did not produce any significant change in the residuals. Both models give $\chi^2 = 42$ for 45 degrees of freedom (dof).
- The replacement of the GABS component by an absorption edge (EDGE) reduced but did not eliminate the residuals at ∼10 keV. The final fit was not acceptable with $\chi^2 = 115$ for 46 dof.
- With the use of Comptonization models, the 10-keV absorption feature becomes insignificant when the parameters (line and width) of the emission line component are let free ($\chi^2 = 36$ for 47 dof). However, in this case, the best-fit line parameters are unrealistic ($E_{\rm Fe} = 6.1 - 6.2$ keV, $\sigma_{\rm Fe} \gtrsim 1.5$ keV) for a component representing fluorescent iron line emission (Giménez-García et al. 2015). In this case, the Gaussian component tries to fit the residuals at ∼10 keV, mimicking the bump model of Klochkov et al. (2007). Fixing the line energy and width to reasonable values, $E_{\rm Fe} = 6.4 - 6.6$ keV and $\sigma_{\rm Fe} \lesssim 0.5$ keV, the Comptonization models cannot account for the deviation from the fit in the range 6-12 keV. The fit can be improved by adding a blackbody component with $kT \approx 1$ keV, that is, without the need for a specific component related to the deficit of photons at 8–10 keV. This is the model used by Galloway et al. (2005). However, even this multi-component model cannot entirely remove the residuals at energies below 10 keV. Reduced $chi^2 \sim 1$ can be obtained provided a larger systematic error of 1% is used , see Galloway et al. (2005).

If the 10 keV feature had a magnetic origin, we would expect to observe variability of the component parameters with pulse phase (Heindl et al. 2004). We performed a pulse phase resolved spectroscopic analysis using observation 70096-01-01-03 (2003-02-12). This observation was chosen because with a total exposure time of 5.1 ks and relatively high intensity, it represents a good compromise between a good signal-to-noise ratio and a high number of pulse cycles. But it also avoids contamination between neighbouring phase bins owing to the uncertainty in the spin period that a longer observations might introduce. First, the pulse period has to be determined. To this end, we extracted a light curve with a time resolution of 2^{-8} s using *GoodXenon* event data. The light curve was divided into 256-s segments, and for each segment we obtained the pulse profile by folding the light curve on a trial period. Taking the first profile as reference, we cross-correlated each profile with the reference profile.

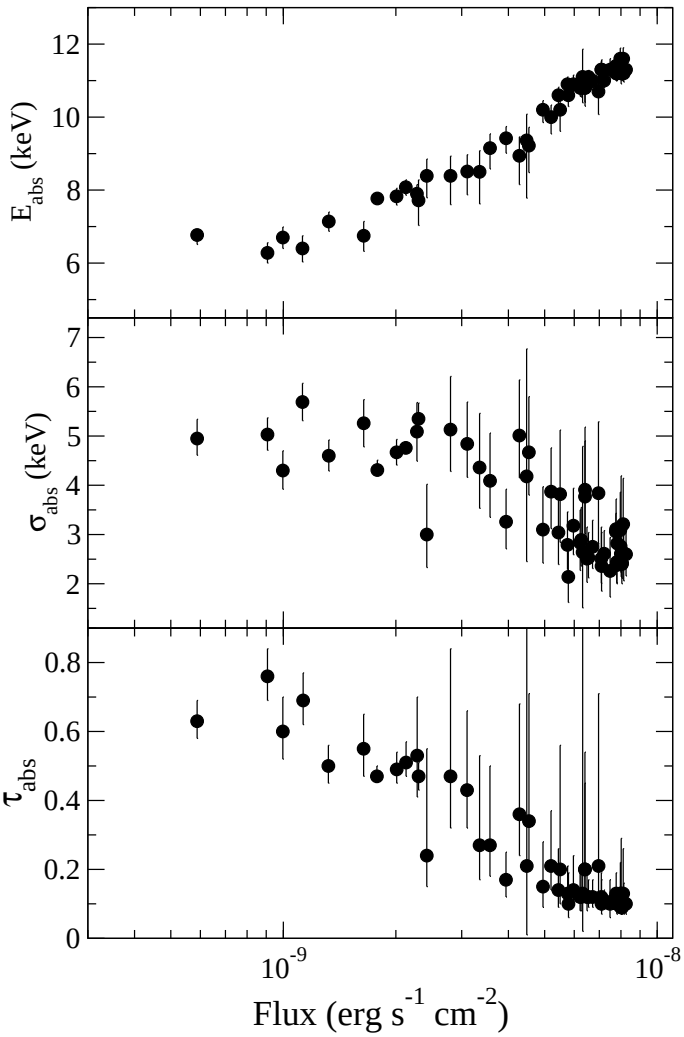

Fig. 7. Evolution of the 10 keV feature parameters with X-ray flux (3–30 keV).

The slope of the linear fit of the time shifts with respect to the mid-time of the segments provided by the correction for the trial period. We repeated the procedure until the data points did not show any trend. The final pulse period was 2.762410 ± 0.000031 s. The pulse profile was divided into six equally spaced bins to provide six 2.9–20 keV spectra. Each spectrum was fitted with the same model as the phase-average spectra of Sect. 3.2. We fixed the hydrogen column density and the iron line and width to their average values, namely, $N_H = 3.3 \times 10^{22}$ cm^{-2}, $E_{\rm Fe} = 6.5$ keV, and $\sigma_{\rm Fe} = 0.5$ keV. A phase modulation is clearly seen in the centroid energy of the 10 keV feature (Fig. 8).

4. Discussion

4.1. Spectral states

Be/X-ray pulsars that go through large amplitude changes in luminosity exhibit spectral states when the source luminosity is significantly higher than the critical luminosity (Reig & Nespoli 2013). The critical luminosity indicates whether the radiation pressure of the emitting plasma is capable of decelerating the accretion flow (Basko & Sunyaev 1976; Becker et al. 2012; Mushtukov et al. 2015a). The critical luminosity defines two accretion regimes. If $L_X > L_{\rm crit}$ (super-critical regime), then radiation pressure is so high that is capable of stopping the accret-

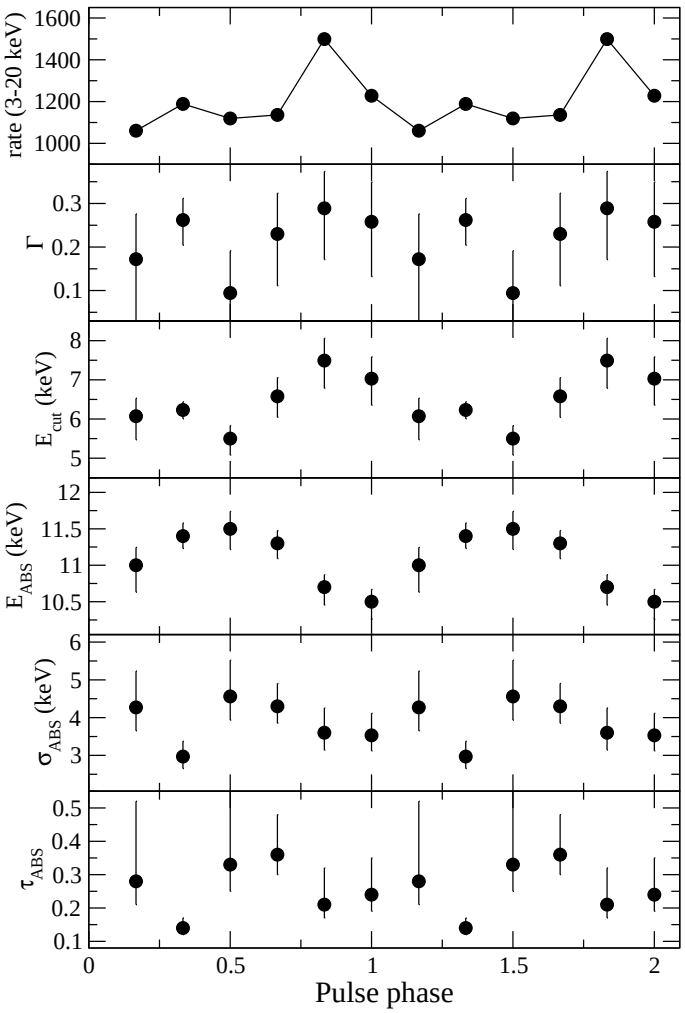

Fig. 8. Variability of the spectral parameters with pulse phase for observation 70096-01-01-03. Shown are 1σ errors.

ing matter at a certain distance above the neutron star surface, which formes a radiation-dominated shock. If $L_X < L_{\rm crit}$ (sub-critical regime), then the accreting material reaches the neutron star surface, heating it through Coulomb collisions with thermal electrons or through nuclear collisions with atmospheric protons (Harding 1994).

Super-critical sources trace two distinct branches in their HID that were called horizontal and diagonal branches (Reig 2008; Reig & Nespoli 2013). The horizontal branch corresponds to a low-intensity state that the source traces during the beginning and end of the outburst, and it is characterised by fast colour and spectral changes and high X-ray variability. The diagonal branch is a high-intensity state that emerges when the X-ray luminosity exceeds the critical limit. To clearly distinguish two branches in the HID, $L_{\rm peak}/L_{\rm crit} >> 1$ and the source luminosity must remain above the critical luminosity long enough so that the observations can sample this high state. Reig & Nespoli (2013) also found that the photon index anti-correlates with X-ray flux in the horizontal branch, but correlates with it in the diagonal branch. Thus the critical luminosity may be estimated by measuring the flux at the break that marks the transition between branches in the HID or at the point where the slope changes in the X-ray flux versus photon index diagram.

In contrast to 4U 0115+63, EXO 2030+375, V 0332+53 or KS 1947+300 (see Fig. 4 in Reig 2008) and (Fig. 6 in Reig & Nespoli 2013), the HID of 4U 1901+03 does not show the two distinct branches (Fig. 3), nor does the photon index show a clear change from negative to positive correlation with flux (Fig. 4). This indicates that 4U 1901+03 remained in the sub-critical regime most of the time. The variability in the pulse profiles confirms this result. In the super-critical regime, X-ray photons are expected to escape the accretion column from the sides, that is, perpendicular to the magnetic field, radiating in a fan beam. In the sub-critical regime, the photons escape parallel to the magnetic field in a pencil beam. These types of complex changes in the pulse profile with luminosity have been seen in other X-ray pulsars (Parmar et al. 1989; Mukerjee et al. 2000; Sasaki et al. 2012; Malacaria et al. 2015). In 4U 1901+03, a double-peak pulse profile is observed. However, the relative strength of the two pulses of the double-pulse profile at low flux reversed compared to the double peak structure at high flux (Chen et al. 2008). This result was interpreted in terms of a luminosity-dependent emission profile of the pulsar, where the emission pattern changes from being dominated by the fan beam at high flux to correspond to a pencil beam at low flux (Mukerjee et al. 2000; Chen et al. 2008). The mixed contribution of fan and pencil beams even at the highest luminosity (Chen et al. 2008) implies that the source was not in a pure super-critical regime, which would be characterised a a fan beam only (see Fig. 1 in Becker et al. 2012).

On the other hand, a flattening toward the peak of the outburst is observed in the $F_X - \Gamma$ relation (see Fig. 4), which might indicate that the source reached the critical luminosity close to the peak of the outburst. Both the HID and the $F_X - \Gamma$ diagram resemble that of XTE J0658–073 (see Fig. 3 in Reig & Nespoli 2013). The similarity between 4U 1901+03 and XTE J0658–073 is reinforced by the fact that the two sources display X-ray flaring behaviour during the peak of the outburst (James et al. 2011; Nespoli et al. 2012). For XTE J0658–073, Reig & Nespoli (2013) argued that $L_{\rm peak}/L_{\rm crit} \gtrsim 1$ but that the source did not remain in the super-critical regime for a substantial period of time, hence it could not develop a clear diagonal branch. The same situation is likely to have occurred in 4U 1901+03.

4.2. 10 keV feature

A peculiar feature in the X-ray energy spectra of 4U 1901+03 is an absorption-line-like profile whose energy varies in the range 6–12 keV (Fig. 6). After fitting the X-ray spectra with a power law, many X-ray pulsars leave significant residuals around 10 keV. This feature is generally referred to as the 10 keV feature (Coburn et al. 2002). Although it appears to be a common feature in many X-ray pulsars, its origin and nature are not known. An instrumental origin is ruled out because it has been observed with different instruments onboard *RXTE*, *Ginga* and *BeppoSAX* (Coburn et al. 2002, and references therein). Because there is no distinct variability pattern, it is difficult to interpret. We summarise the most relevant characteristics of this feature below.

- It may be modelled as an emission feature as in 4U 0115+63 (Ferrigno et al. 2009; Müller et al. 2013) and EXO 2030+375 (Klochkov et al. 2007), or as an absorption feature as in XTE J0658-073 (McBride et al. 2006; Nespoli et al. 2012) or XTE J1946+274 (Müller et al. 2012). In either case, a Gaussian profile is used (see Table 1 for the functional form of these components).
- The feature has been observed regardless of whether a cyclotron line is present or not. This led Coburn et al. (2002) to

conclude that the component probably is not a magnetic effect. It may easily be mistaken as a cyclotron line. For example, in EXO 2030+375, this additional broad emission component is not needed when two absorption lines at ∼10 keV and ∼20 keV are used (Klochkov et al. 2007), which could be interpreted as cyclotron lines (Wilson et al. 2008).
- The central energy of the feature does not generally vary in time or flux (Nespoli et al. 2012; Müller et al. 2012), although a weak anti-correlation with flux was reported by Müller et al. (2013) in 4U 0115+63.

Theory predicts that the energy of the cyclotron line observed in many accreting pulsars shows a positive correlation with flux when the pulsar is in the sub-critical regime and a negative correlation in the super-critical regime (Becker et al. 2012; Nishimura 2014; Mushtukov et al. 2015b). In the previous section we argued that the source is in the sub-critical regime most of the time. The positive correlation of the energy of the absorption feature with flux that we measure in 4U 1901+03 (Fig. 7) would support the association of the 10 keV feature with a cyclotron line. The width and depth of the feature are also typical of accreting pulsars (Coburn et al. 2002). The shape of cyclotron lines in accreting X-ray pulsars depends strongly on the viewing angle, hence on the pulse phase (Isenberg et al. 1998; Araya-Góchez & Harding 2000; Heindl et al. 2004). Additional support for the interpretation of the 10 keV feature as a cyclotron line therefore comes from the variation of the feature parameters with pulse phase (Fig. 8).

On the other hand, if this feature were a cyclotron line, then the critical luminosity would be of the order of 10^{37} erg s^{-1} (Becker et al. 2012; Mushtukov et al. 2015a). Thus not only $L_{\rm peak}/L_{\rm crit} \sim 8$ (assuming a distance of 10 kpc), but also $L_X/L_{\rm crit} > 1$ for most part of the outburst, and a distinct diagonal branch should be observed in the HID. We note, however, that this conclusion is based on a rather uncertain distance. A distance larger than ∼ 8 kpc would argue against the 10 keV feature as a cyclotron line because $L_X/L_{\rm crit} > 1$. To have $L_{\rm peak}/L_{\rm crit} \sim 1$, the distance to the source should not be larger than ∼4 kpc. At this distance, an early-type B star should be easily detectable with photometric observations, unless the optical extinction is very high, $A_V \gtrsim 10$ mag. The relatively high column density of the spectral fits supports high extinction toward the source.

In summary, the inclusion of an absorption component to account for the residuals at 8–10 keV provides acceptable fits even with a small systematic error of 0.6%. The variability of the energy of this component with flux and with pulse phase and the persistence of the residuals regardless of the continuum model used is reminiscent of a CRSF. However, the lack of a reliable distance estimate prevents us from establishing a connection between this feature and accretion models.

4.3. Transition to the propeller regime

Figure 3 shows the light curve of 4U 1901+03. The duration of the decay phase of the outbursts (from peak to last observation) was ∼ 150 days. The source displays several sudden decreases in flux over the course of the decay. These abrupt changes in luminosity are apparent in the HID, where a clear change in the slope of the curve is seen, implying a major change in the physical conditions of the emission region.

The most significant changes in terms of the fractional amplitude of flux ($f_{i+1} - f_i)/f_i$) occurred towards the end of the outburst. In particular, the largest change took place between MJD 52830-58832 (bottom panel in Fig. 3). These abrupt changes

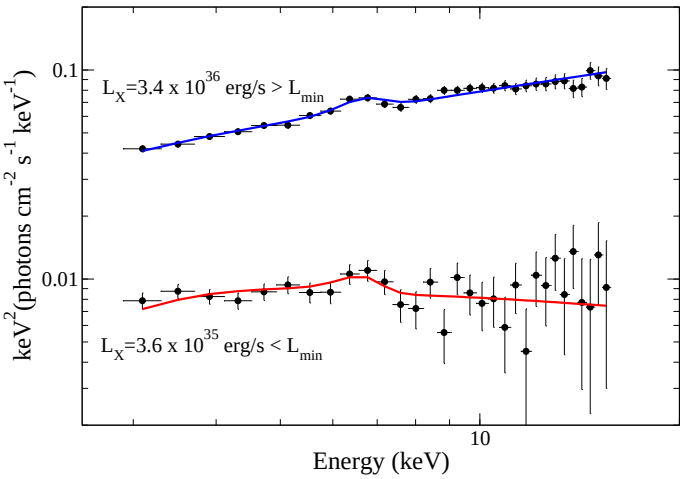

Fig. 9. X-ray spectrum of 4U 1901+03 in the accretor (top) and propeller (bottom) states.

in luminosity have been attributed to a change in the accretion regime whereby the source transits from an accretor state to the propeller state (Illarionov & Sunyaev 1975; Stella et al. 1986), which has been observed in a number of pulsars (Cui 1997; Campana et al. 2001, 2002; Tsygankov et al. 2016).

In the process of mass accretion, the ram pressure of the flow is exerted on the magnetosphere and is balanced by the magnetic pressure. Therefore, the size of the magnetosphere is determined not only by field strength but also by mass accretion rate. In a bright state, the accretion rate is high, so that the magnetosphere is usually small compared to the co-rotation radius at which the angular velocity of Keplerian motion is equal to that of the neutron star. Material is continuously channelled to magnetic poles, and the X-ray emission from hot spots pulsates. As the accretion rate decreases, the ram pressure decreases, and thus the magnetosphere expands. As the magnetosphere grows beyond the co-rotation radius, the centrifugal force prevents material from entering the magnetosphere, and thus accretion onto magnetic poles ceases. This is commonly known as the propeller effect (Illarionov & Sunyaev 1975; Stella et al. 1986).

There exists a lowest X-ray luminosity, determined by the lowest accretion rate, below which the propeller effect sets in (see e.g. Campana et al. 2002),

$$L_{\rm min}(R_{\rm NS}) = 3.9 \times 10^{37} k^{7/2} B_{12}^2 P_{\rm s}^{-7/3} M_{1.4}^{-2/3} R_6^5 \ {\rm erg\,s^{-1}}, \quad (1)$$

where k is a constant that accounts for the geometry of the flow. $k \approx 1$ in case of spherical accretion and $k \approx 0.5$ in case of disk accretion. B_{12} is the magnetic field strength in units of 10^{12} G, $P_{\rm s}$ the spin period in seconds, and $M_{1.4}$ and R_6 the mass and radius of the neutron star in units of 1.4 $M_\odot$ and 10^6 cm, respectively. Below this limiting luminosity, the accreting matter can no longer reach the neutron star surface because it is spun away by the fast rotation of the magnetosphere. For rapid-rotating pulsars ($P_{\rm spin} \sim 1$ s), $L_{\rm min}(R_{\rm NS})$ is relatively high, $\sim 10^{36}$ erg s^{-1}. For long-pulsing systems ($P_{\rm spin} \sim 100$ s), $L_{\rm min}(R_{\rm NS}) \sim 10^{32} - 10^{33}$ erg s^{-1} (Stella et al. 1986; Campana et al. 2001; Reig et al. 2014; Tsygankov et al. 2016). Assuming the typical mass and radius of a neutron star, $k = 1$, and a magnetic field of $\sim (3-5) \times 10^{11}$ G (Galloway et al. 2005; James et al. 2011), the lowest luminosity in 4U 1901+03 is $L_{\rm min} \sim (4-9) \times 10^{35}$ erg s^{-1}. For a distance of 8–10 kpc, this luminosity corresponds to a flux of $(0.4-1.2) \times 10^{-10}$ erg s^{-1} cm^{-2}. The horizontal dashed line in Fig. 3 indicates this limiting flux.

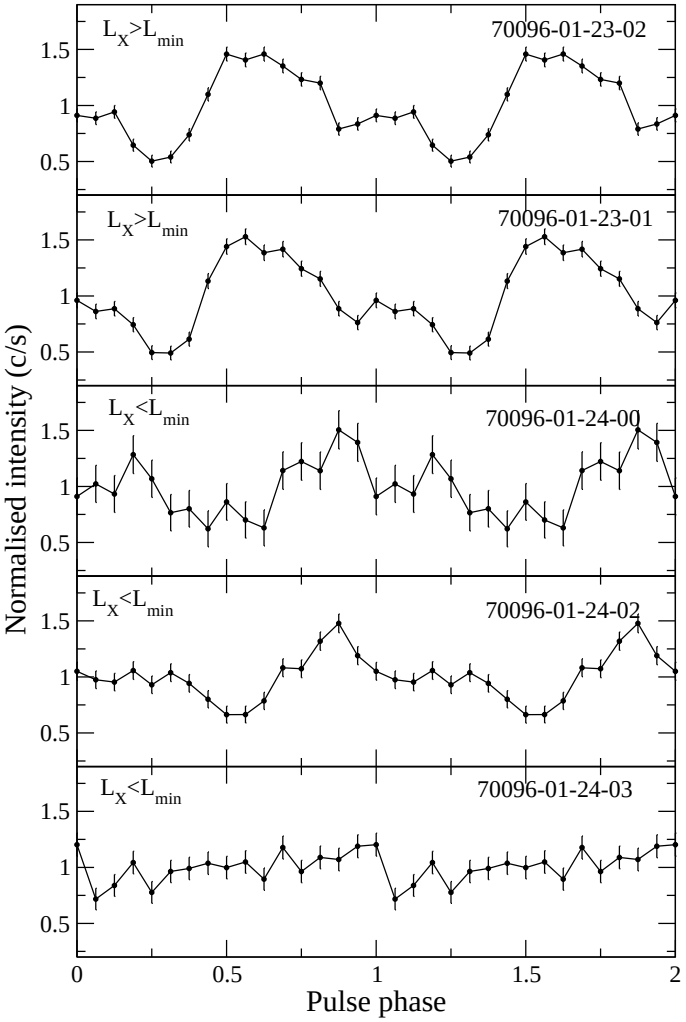

Fig. 10. Pulse profiles as a function of luminosity. Below $L_{\rm min}$ the X-ray pulsations vanish.

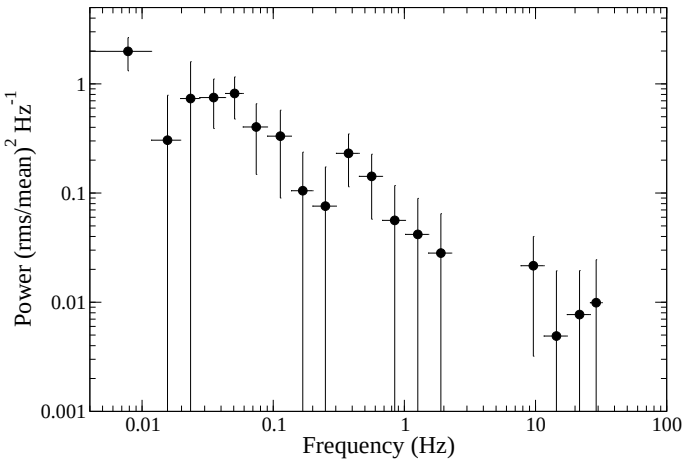

Fig. 11. Power spectrum of 4U 1901+03 in the propeller state in the energy range 3–15 keV.

To investigate the emission properties in this low state, we performed a spectral and timing analysis on the last five observations (MJD 52832–52837). Figure 9 shows the energy spectra of 4U 1901+03 above and below the limiting luminosity, given by Eq. (1). At $L_X < L_{\rm min}$, the spectra are significantly softer and consistent with a power law with $\Gamma \sim 2.1$, compared to $\Gamma \sim 1.5$ in the accretor state. To increase the signal-to-noise ratio of the spectra with $L_X < L_{\rm min}$, we obtained the average spectrum of the last five observations ($F_x < 5 \times 10^{-11}$ erg s^{-1} cm^{-2}). The 2.5-15 keV spectrum is well described by a single power law with the best-fit photon index $\Gamma \sim 2.0 \pm 0.1$, giving $\chi^2 = 24.3$ for 32 degrees of freedom. Tsygankov et al. (2016) also found substantial softening of the *Swift*/XRT spectra in the propeller state of the BeXBs 4U 0115+63 and V 0332+53. These authors found that an absorbed blackbody with $kT \approx 0.5$ keV described the low-state spectra well. However, given the very narrow energy range fitted in the *Swift*/XRT spectrum, a power-law distribution cannot be completely ruled out. A blackbody does not provide a good fit of the low-flux spectra in 4U 1901+03 as a result of excess emission above 10 keV.

Figure 10 shows the pulse profiles at various luminosities. X-ray pulsations are detected even below $L_{\rm min}$. The last significant (at 99% confidence level) detection of pulsations occurred for observation 70096-01-24-02 (MJD 52833.2, $f_x = 3.1 \times 10^{-11}$ erg s^{-1} cm^{-2}), while for 70096-01-24-01 (MJD 52834.2, $f_x = 2.7 \times 10^{-11}$ erg s^{-1} cm^{-2}) is only marginal at 90% confidence level. Below this flux, no pulsations are detected. The decrease in X-ray pulse fraction when the source flux drops below a certain threshold has been interpreted as due to the propeller effect (Cui 1997; Campana et al. 2001). The average power spectrum in the low state is shown in Fig. 11. Power-law noise is clearly detected. The best-fit power-law index is 0.8 ± 0.2 and the rms variability in the frequency range 0.01–10 Hz is $\sim 40\%$.

The onset of the propeller regime does not mean that the X-ray emission is halted. Even pulsation may be detected during quiescence (Rutledge et al. 2007). Several models have been put forward to explain the X-ray emission at low luminosities. For example, a fraction of matter may still leak through the barrier (Doroshenko et al. 2011). Alternatively, high-energy radiation may also be detected as a thermal spectrum, which likely originates in the polar caps of the neutron star surface heated during intermittent accretion episodes or by non-uniform cooling of the neutron star surface after a recent outburst (Reig et al. 2014; Tsygankov et al. 2016). Deep crustal heating, where the crust of the neutron star cools by X-ray emission until it reaches thermal equilibrium, can also account for the emission at quiescence (Brown et al. 1998; Wijnands et al. 2013). In these cases, the X-ray luminosity is expected to be $L_{\rm th} \lesssim 10^{33}$ erg s^{-1}. These scenarios are ruled out by the observations for 4U 1901+03. First, the X-ray spectrum in the low (propeller) state is not blackbody (thermal). Second, the luminosity is significantly higher than $L_{\rm th}$. Finally, the power spectrum of 4U 1901+03, obtained from the five observations with $L_x < L_{\rm min}$, exhibits strong low-frequency noise and broadband rms variability (Fig. 11). A flat spectrum (white noise), that is, an absence of variability, is expected in the case of emission from hot polar caps (Reig et al. 2014, and references therein).

Another mechanism that can produce X-rays when the centrifugal barrier is at work is magnetospheric accretion (King & Cominsky 1994; Campana et al. 1995; Corbet 1996). In this scenario, gravitational energy is released by accreting material that is deposited in the magnetosphere. X-ray pulsations may still be produced by the azimuthal asymmetry of the rotating magnetospheric boundary. On first approximation, the accreted luminosity will be driven by the same mass transfer as in the accretor regime, but with the magnetospheric radius replacing the neutron star radius $L_m \approx GM_{\rm NS}\dot{M}/R_m$. The highest luminosity in this regime will occur when the magnetospheric radius equals

the co-rotation radius $R_m = R_{\rm co} = (GM_{\rm NS}P_{\rm s}^2)^{1/3}/4\pi^2$. Hence (Campana et al. 2002)

$$L_{\rm min}(R_m) = 2.4\times10^{35}k^{7/2}B_{12}^2P_{\rm s}^{-3}M_{1.4}^{-1}R_6^6 \ {\rm erg\,s^{-1}}. \quad (2)$$

This luminosity also represents the level at which the propeller barrier closes completely. The lowest X-ray luminosity in 4U 1901+03, $L_{X,\rm min} \sim 10^{35}$ erg s^{-1}, is still considerably higher than the highest luminosity that can be emitted in the propeller regime as given by Eq. (2).

Unfortunately, *RXTE* was not sensitive to faint observations. The source became too faint for the sensitivity of the detectors. The observations of 4U 1901+03 stopped before the propeller barrier closed completely. Although the source did enter the propeller accretion regime, it did not reach a stable configuration that would allow us to distinguish between different emission scenarios in quiescence.

5. Conclusion

We have performed a timing and spectral X-ray analysis of 4U 1901+03 during the 2003 outburst. As the X-ray flux decreases from the peak of the outburst to quiescence, the source enters different accretion regimes. At the highest flux, the X-ray luminosity of 4U 1901+03 may have briefly reached the critical luminosity, and the source may have entered the super-critical accretion regime. However, the absence of a diagonal branch in the hardness-intensity diagram and the absence of a shift from anti-correlation to correlation in the flux vs photon index diagram indicate that 4U 1901+03 was in the sub-critical state most of the time. At the end of the outburst, when the flux decreased below $\sim 10^{-10}$ erg cm^{-2} s^{-1}, the source entered the propeller regime. In this state, the spectra became softer and the X-ray pulsation vanished. Unfortunately, the source flux at the end of the outbursts reached the sensitivity limit of the instruments and the observations ended before a stable quiescent state was reached. The lower-flux observations of 4U 1901+03 represent a transition state between the onset of the propeller effect and quiescence. Based on the positive correlation of the energy of this component with X-ray flux and pulse phase, we tentatively associate the 10 keV feature with a cyclotron line. The discovery of the optical counterpart and the determination of the distance will solve the question of whether 4U 1901+03 entered the super-critical regime during the 2003 outburst.

Acknowledgements. Skinakas Observatory is a collaborative project of the University of Crete and the Foundation for Research and Technology-Hellas. This publication makes use of data products from the Two Micron All Sky Survey, which is a joint project of the University of Massachusetts and the Infrared Processing and Analysis Center/California Institute of Technology, funded by the National Aeronautics and Space Administration and the National Science Foundation. This work has made use of NASA's Astrophysics Data System Bibliographic Services and of the SIMBAD database, operated at the CDS, Strasbourg, France. This research has made use of MAXI data provided by RIKEN, JAXA and the MAXI team.

References

Anders, E. & Grevesse, N. 1989, Geochim. Cosmochim. Acta, 53, 197
Araya-Góchez, R. A. & Harding, A. K. 2000, ApJ, 544, 1067
Arnaud, K. A. 1996, in Astronomical Society of the Pacific Conference Series, Vol. 101, Astronomical Data Analysis Software and Systems V, ed. G. H. Jacoby & J. Barnes, 17
Balucinska-Church, M. & McCammon, D. 1992, ApJ, 400, 699
Basko, M. M. & Sunyaev, R. A. 1976, MNRAS, 175, 395
Becker, P. A., Klochkov, D., Schönherr, G., et al. 2012, A&A, 544, A123
Bessell, M. S. 1990, PASP, 102, 1181
Brown, E. F., Bildsten, L., & Rutledge, R. E. 1998, ApJ, 504, L95
Campana, S., Gastaldello, F., Stella, L., et al. 2001, ApJ, 561, 924
Campana, S., Stella, L., Israel, G. L., et al. 2002, ApJ, 580, 389
Campana, S., Stella, L., Mereghetti, S., & Colpi, M. 1995, A&A, 297, 385
Chen, W., Qu, J.-l., Zhang, S., Zhang, F., & Zhang, G.-b. 2008, Chinese Astron. Astrophys., 32, 241
Coburn, W., Heindl, W. A., Rothschild, R. E., et al. 2002, ApJ, 580, 394
Corbet, R. H. D. 1986, MNRAS, 220, 1047
Corbet, R. H. D. 1996, ApJ, 457, L31
Cui, W. 1997, ApJ, 482, L163
Doroshenko, V., Santangelo, A., & Suleimanov, V. 2011, A&A, 529, A52
Farinelli, R., Ceccobello, C., Romano, P., & Titarchuk, L. 2012, A&A, 538, A67
Ferrigno, C., Becker, P. A., Segreto, A., Mineo, T., & Santangelo, A. 2009, A&A, 498, 825
Forman, W., Tananbaum, H., & Jones, C. 1976, ApJ, 206, L29
Galloway, D., Remillard, R., Morgan, E., & Swank, J. 2003, IAU Circ., 8070
Galloway, D. K., Wang, Z., & Morgan, E. H. 2005, ApJ, 635, 1217
Giménez-García, A., Torrejón, J. M., Eikmann, W., et al. 2015, A&A, 576, A108
Harding, A. K. 1994, in American Institute of Physics Conference Series, Vol. 308, The Evolution of X-ray Binariese, ed. S. Holt & C. S. Day, 429
Heindl, W. A., Rothschild, R. E., Coburn, W., et al. 2004, in American Institute of Physics Conference Series, Vol. 714, X-ray Timing 2003: Rossi and Beyond, ed. P. Kaaret, F. K. Lamb, & J. H. Swank, 323–330
Hua, X.-M. & Titarchuk, L. 1995, ApJ, 449, 188
Illarionov, A. F. & Sunyaev, R. A. 1975, A&A, 39, 185
Isenberg, M., Lamb, D. Q., & Wang, J. C. L. 1998, ApJ, 505, 688
Jahoda, K., Markwardt, C. B., Radeva, Y., et al. 2006, ApJS, 163, 401
James, M., Paul, B., Devasia, J., & Indulekha, K. 2011, MNRAS, 410, 1489
Jaschek, C. & Jaschek, M. 1987, The classification of stars
Jenke, P. & Finger, M. H. 2011, The Astronomer's Telegram, 3839
King, A. & Cominsky, L. 1994, ApJ, 435, 411
Klochkov, D., Horns, D., Santangelo, A., et al. 2007, A&A, 464, L45
Lei, Y.-J., Chen, W., Qu, J.-L., et al. 2009, ApJ, 707, 1016
Levine, A. M., Bradt, H., Cui, W., et al. 1996, ApJ, 469, L33
Malacaria, C., Klochkov, D., Santangelo, A., & Staubert, R. 2015, A&A, 581, A121
McBride, V. A., Wilms, J., Coe, M. J., et al. 2006, A&A, 451, 267
Molkov, S., Lutovinov, A., & Grebenev, S. 2003, A&A, 411, L357
Morrison, R. & McCammon, D. 1983, ApJ, 270, 119
Mukerjee, K., Agrawal, P. C., Paul, B., et al. 2000, A&A, 353, 239
Müller, S., Ferrigno, C., Kühnel, M., et al. 2013, A&A, 551, A6
Müller, S., Kühnel, M., Caballero, I., et al. 2012, A&A, 546, A125
Mushtukov, A. A., Suleimanov, V. F., Tsygankov, S. S., & Poutanen, J. 2015a, MNRAS, 447, 1847
Mushtukov, A. A., Tsygankov, S. S., Serber, A. V., Suleimanov, V. F., & Poutanen, J. 2015b, MNRAS, 454, 2714
Negueruela, I. & Schurch, M. P. E. 2007, A&A, 461, 631
Nespoli, E., Reig, P., & Zezas, A. 2012, A&A, 547, A103
Nishimura, O. 2014, ApJ, 781, 30
Parmar, A. N., White, N. E., & Stella, L. 1989, ApJ, 338, 373
Paul, B. & Naik, S. 2011, Bulletin of the Astronomical Society of India, 39, 429
Postnov, K. A., Gornostaev, M. I., Klochkov, D., et al. 2015, MNRAS, 452, 1601
Poutanen, J., Mushtukov, A. A., Suleimanov, V. F., et al. 2013, ApJ, 777, 115
Reig, P. 2008, A&A, 489, 725
Reig, P., Doroshenko, V., & Zezas, A. 2014, MNRAS, 445, 1314
Reig, P., Negueruela, I., Papamastorakis, G., Manousakis, A., & Kougentakis, T. 2005, A&A, 440, 637
Reig, P. & Nespoli, E. 2013, A&A, 551, A1
Rothschild, R. E., Blanco, P. R., Gruber, D. E., et al. 1998, ApJ, 496, 538
Rutledge, R. E., Bildsten, L., Brown, E. F., et al. 2007, ApJ, 658, 514
Sasaki, M., Müller, D., Kraus, U., Ferrigno, C., & Santangelo, A. 2012, A&A, 540, A35
Skrutskie, M. F., Cutri, R. M., Stiening, R., et al. 2006, AJ, 131, 1163
Sootome, T., Nakajima, M., Mihara, T., et al. 2011, The Astronomer's Telegram, 3829
Stella, L., White, N. E., & Rosner, R. 1986, ApJ, 308, 669
Titarchuk, L. 1994, ApJ, 434, 570
Torrejón, J. M., Schulz, N. S., Nowak, M. A., & Kallman, T. R. 2010, ApJ, 715, 947
Tsygankov, S. S., Lutovinov, A. A., Doroshenko, V., Mushtukov, A. A., & Poutanen, J. 2016, ArXiv e-prints
Weisskopf, M. C., Guainazzi, M., Jahoda, K., et al. 2010, ApJ, 713, 912
Wijnands, R., Degenaar, N., & Page, D. 2013, MNRAS, 432, 2366
Wilson, C. A., Finger, M. H., & Camero-Arranz, A. 2008, ApJ, 678, 1263